1 **Revision 1**

2 Formation of the Maoniuping giant REE deposit: constraints from
3 mineralogy and *in situ* bastnäsite U–Pb geochronology

4

5 Qiang Weng[1, 2], Wu-Bin Yang[1,*], He-Cai Niu[1], Ning-Bo Li[1], Roger H. Mitchell[3],
6 Shannon Zurevinski[3] and Dan Wu[1]
7 [1]Key Laboratory of Mineralogy and Metallogeny/Guangdong Provincial Key
8 Laboratory of Mineral Physics and Materials, Guangzhou Institute of Geochemistry,
9 Chinese Academy of Sciences, Guangzhou 510640, China
10 [2]University of Chinese Academy of Sciences, Beijing 100049, China
11 [3]Department of Geology, Lakehead University, 955 Oliver Road, Thunder Bay,
12 Ontario P7B 5E1, Canada
13 * Corresponding author. E-mail: yangwubin@gig.ac.cn (W.B. Yang)

14

15 ABSTRACT

16 The time and processes of hydrothermal mineralization are long-standing
17 problems in geology. This work addresses these questions with reference to the
18 Maoniuping giant rare earth elements (REE) deposit (SW China), with rare earth
19 oxides (REO) reserves of 3.17 million tons with an average grade of 2.95 wt.%.
20 Bastnäsite is the dominant economic mineral, occurring as four distinct paragenetic
21 types in the Maoniuping syenite–carbonatite complex: (1) Primary euhedral bastnäsite
22 (type-A) in syenite, with isolated melt inclusions; (2) Macro-crystalline tabular
23 euhedral bastnäsite (type-B) in pegmatitic dikes, with diverse variety of fluid
24 inclusions; (3) Fine-grained, anhedral veinlet-disseminated bastnäsite (type-C) in
25 syenite; (4) Coarse-grained anhedral bastnäsite (type-D) in carbonatite dikes,

occurring as veinlets or interstitial to calcite, fluorite and barite. From the paragenetic and compositional variations, it is inferred that type-A bastnäsite is of primary magmatic origin, whereas the other three types have characteristics of hydrothermal origins. *In situ* LA-ICPMS U–Pb geochronology of the four types of bastnäsite results in lower intercept ages of 28.2 ± 0.5 Ma (*n*=95, MSWD=5.10), 27.8 ± 0.4 Ma (*n*=43, MSWD=0.73), 26.8 ± 0.7 Ma (*n*=50, MSWD=0.83) and 25.8 ± 0.7 Ma (*n*=55, MSWD=1.70), respectively, which are consistent with the weighted average $^{206}Pb/^{238}U$ and $^{208}Pb/^{232}Th$ ages by ^{207}Pb-correction method. Compositional variations of clinopyroxene and apatite from the associated syenite, pegmatitic and carbonatitic dikes indicate a genetic relationship of the Maoniuping alkaline complex. The compositions of clinopyroxene range from $Ae_{44–67}Di_{14–18}Hd_{17–41}$ in pegmatitic dikes, $Ae_{43–66}Di_{6–20}Hd_{21–38}$ in carbonatitic dikes to $Ae_{68–90}Di_{0–3}Hd_{10–30}$ in syenite. Apatites in the pegmatitic and carbonatitic dikes have similar compositions with higher F, total REE and Sr and lower CaO contents than those in the syenite, which suggests a cogenetic origin for the associated pegmatite and carbonatite. Clinopyroxene and apatite compositions suggest that the pegmatitic melt might differentiate directly from the initial carbonatitic melt rather than the syenitic magma. The bastnäsite U–Pb geochronology and minerals data indicate continuous magmatic-hydrothermal evolution for the REE mineralization in the Maoniuping alkaline complex.

Keywords: U–Pb geochronology, bastnäsite, Maoniuping giant REE deposit, syenite–carbonatite complex, magmatic–hydrothermal evolution

INTRODUCTION

Rare earth elements (REE) are known as "Critical Metals", which are crucial to the high-technical industry and national security (Chakhmouradian and Wall 2012). More than half of the global REE reserves identified are associated with alkaline igneous rocks, especially diverse carbonatites (Mitchell 2005; Weng et al. 2015). The REE minerals typically occur in hydrothermal systems, such as Bayan Obo (China, Smith et al. 2000), Gallinas Mountains (USA, Williams-Jones et al. 2000), and Kangankunde (Malawi, Broom-Fendley et al. 2017). In contrast, some REE minerals such as bastnäsite and monazite are formed at purely magmatic and/or magmatic-hydrothermal transitional stages, e.g., Mountain Pass (USA, Mariano 1989; Castor 2008), Lovozero-Khibina (Russia, Zaitsev et al. 2014), Palabora (South Africa, Giebel et al. 2017), Ulgii Khiid (Mongolia, Feng et al. 2020), Strange Lake (Canada, Vasyukova and Williams-Jones 2018) and Baerzhe (China, Yang et al. 2014a). Understanding the genesis of REE minerals is critical to deciphering the processes of REE mineralization in magmatic-hydrothermal deposits.

Bastnäsite [(REE)(CO_3)F] is a common economic mineral in most hydrothermal REE ore deposits related to alkaline-carbonatite complexes (Gysi and Williams-Jones 2015). Bastnäsite is also considered to be a promising U–Pb geochronological tool, because of its significant U (222–653 ppm) content (Sal'nikova et al. 2010; Yang et al. 2014b; Ling et al. 2016). Sal'nikova et al. (2010) conducted the first U–Pb isotopic analysis by thermal ionization mass spectrometry (TIMS) on bastnäsite (K-9) from the Karasug carbonatite in central Mongolia, which yielded a concordant age of 118 ± 1 Ma. Using this K-9 bastnäsite as reference material, Yang et al. (2014b) carried out bastnäsite U–Pb age determination by *in situ* Laser Ablation Inductively Coupled Plasma Mass Spectrometry (LA-ICPMS). With respect to the high Th (1,161–4,165

ppm) content, Ling et al. (2016) proposed an alternative protocol for *in situ* bastnäsite Th–Pb analysis and data calibration by secondary ion mass spectrometry (SIMS). Therefore, it is suggested that bastnäsite U (Th)–Pb geochronology would have potential to determine accurately the timing of REE mineralization.

Maoniuping is the second largest REE deposit in China, with reserves of 3.17 Mt rare earth oxides (REO) @ 2.95 wt.% (109 Geological Brigade of Sichuan Bureau of Geology and Mineral Resource 2010). Previous studies of the Maoniuping deposit gave zircon U–Pb ages of 21–27 Ma (Liu et al. 2015; Ling et al. 2016), biotite and arfvedsonite K(Ar)/Ar ages of 26–40 Ma (Yuan et al. 1995; Liu and Hou 2017; Liu et al. 2019a), and bastnäsite U–Pb and Th–Pb ages of 31.9±3.9 Ma and 25.7±0.2 Ma, respectively (Yang et al. 2014b; Ling et al. 2016). Such large discrepancies have led to controversy concerning the genesis of the deposit. For example, Pu (1993) proposed that the fluids responsible for the REE mineralization are genetically related to the syenite intrusion. Niu and Lin (1994) suggested that the REE mineralization is possibly induced by immiscibility between sulfate and carbonate salt melts. Xie et al. (2015) and Hou et al. (2015) considered that the REE-enriched fluids mainly originate from the carbonatite rather than the syenite. More recently, Liu et al. (2019b) determined that the ore-forming fluids are essentially derived from the syenite-carbonatite complex. To address these genetic disputes, we directly determine the age of bastnäsite of different parageneses by *in situ* LA-ICPMS U–Pb method. In combination with the geochronology and mineral compositions as determined by EMPA and LA-ICPMS, a possible genetic model for the formation of the Maoniuping giant REE deposit is proposed.

GEOLOGICAL BACKGROUND

Regional geology

The on-going India–Asia continental collision event began at ca. 65 Ma affected an extensive area beyond the Tibetan plateau (Fig. 1a; Yin and Harrison 2000; Hou et al. 2003; Hou and Cook 2009). This intensive interaction between the India and Asia continents resulted in clusters of collisional orogenic belts in the east of the Tibetan plateau, including the N–S striking Jinpingshan orogeny. The Panxi (Panzhihua-Xichang city) REE metallogenic belt is located in the eastern part of the Jinpingshan orogeny, and related to a series of Cenozoic N–S trending strike-slip faults. Numerous Cenozoic alkaline–peralkaline igneous rocks have been documented in this belt, such as lamprophyre (40–24 Ma, Guo et al. 2005), alkaline syenitic rocks, and syenite-carbonatite complexes (30–11 Ma, Xie et al. 2016). The Panxi REE metallogenic belt, 270 km in length and 15 km in width, runs north from Mianning, through Xichang and Dechang to Panzhihua. Within this belt there are four known economic REE deposits, i.e., Maoniuping, Dulucao, Muluo and Lizhuang, and some REE ore occurrences (Yuan et al. 1995). Most of these are lithology-related to the syenite–carbonatite complexes intruded as stocks or dikes into the Precambrian crystalline basement, Mesozoic alkaline granite and a Paleozoic to Mesozoic volcano–sedimentary sequence (Yuan et al. 1995). The REE deposits are spatially controlled by the N–S trending Anninghe strike-slip fault (Yuan et al., 1995).

Ore deposit geology

The Maoniuping area consists of four main lithological units, including Mesozoic alkaline granite, rhyolite with unknown age, Devonian to Permian sedimentary rocks, and the ore-bearing alkaline complex of syenite stocks and pegmatitic-carbonatitic dikes (Fig. 1b). The syenite–carbonatite complex intruded the rhyolite and Mesozoic alkaline granite (Fig. 1b). The REE mineralization at Maoniuping district occurs as the

vein systems hosted in syenite, carbonatite, and to a lesser extent, altered granite and rhyolite. The REE minerals in the ore bodies are predominantly bastnäsite. The ores consist of REE-enriched veinlets, stringers, and stock-work zones which surround the carbonatite and the ores occur mainly as disseminations in syenite, pegmatitic dikes, secondary veinlets in syenite and carbonatitic dikes. More than 71 pegmatitic and carbonatitic dikes have been identified with widths ranging from 1 to 30m and lengths from 10 to 1200m (Yuan et al. 1995). They show a NNE orientation, with an "S-like" shape (Fig. 1b).

Currently, there are two open pits in operation, Dagudao and Guangtoushan. In the Dagudao open pit, dark-coloured pegmatitic dikes intruded into the syenite stock. These pegmatitic dikes are the main ore type. In contrast, the pink carbonatitic dikes are the main ore type in the Guangtoushan open pit. In this study, rock and mineral samples of unaltered and altered syenite were collected from the Dagudao open pit. Ore samples of pegmatitic and carbonatite dikes are from the Guangtoushan open pits (Fig. 1b).

PETROGRAPHY

The grayish-white, medium-grained syenite is the predominant intrusive rock in the Maoniuping alkaline complex. It is composed mainly of euhedral alkali-feldspar (65–75 vol.%) and subhedral- to- anhedral quartz (20–25 vol.%), with minor aegirine, arfvedsonite and biotite (Fig. 2a). The pegmatite is composed of variable volumes of barite (30–50 vol.%), aegirine-augite and arfvedsonite (30–40 vol.%), fluorite (10–20 vol.%) and bastnäsite (10–20 vol.%), with minor calcite, biotite, apatite, feldspar and quartz (Fig. 2b). The veinlets hosted in syenite are composed mainly of aegirine-augite (40–60 vol.%), fluorite (20–30 vol.%), and bastnäsite (10–15 vol.%) (Fig. 2c). The pink coarse-grained carbonatite is composed mostly of euhedral calcite (50–80 vol.%),

146 barite (10–20 vol.%), fluorite (10–20 vol.%), aegirine-augite and arfvedsonite (5–15
147 vol.%), bastnäsite (5–10 vol.%), with minor biotite, feldspar and quartz (Fig. 2d).

148 Bastnäsite is the main economic mineral in the unaltered syenite, the pegmatitic
149 and carbonatite dikes and the secondary veinlets in syenite. Bastnäsite in the unaltered
150 syenite has a hexagonal euhedral habit and occurs within euhedral orthoclase (Fig. 3a).
151 Rounded isolated melt inclusions can be found in this type of bastnäsite (Fig. 3b),
152 referred as "type-A bastnäsite". In the pegmatites, euhedral- to -subhedral bastnäsite
153 occurs as a tabular mineral (Fig. 3c) with primary fluid inclusions ("type-B bastnäsite",
154 Fig. 3d). Bastnäsite from the secondary veinlets hosted in syenite is anhedral or
155 euhedral (Fig. 3e), and contains numerous primary fluid inclusions (Fig. 3f), and
156 referred as "type-C bastnäsite". Bastnäsite ("type-D bastnäsite"), in the carbonatite
157 dikes is commonly euhedral- to- subhedral with fluid inclusions (Figs. 3g and 3h).

158 Clinopyroxene and apatite are the pervasive minerals in the Maoniuping
159 syenite-carbonatite complex. Clinopyroxene is augite-aegirine in the alkaline complex
160 and in the syenite is mostly euhedral, prismatic, and closely associated with orthoclase,
161 biotite and quartz (Fig. 4a). In some examples, euhedral clinopyroxene occurs as
162 inclusions hosted by orthoclase. Euhedral clinopyroxenes from the pegmatitic and
163 carbonatite dikes are large- to- megacrystic in size (3-6 mm), and closely associated
164 with barite and calcite (Figs. 4b and 4c). Apatite in the syenite is mainly euhedral, and
165 occurs as prismatic or hexagonal crystals (Fig. 4d). Apatite is rare in the pegmatitic
166 and carbonatite dikes, and can occur as inclusions within clinopyroxene and calcite
167 (Figs. 4e and 4f).

168 **ANALYTICAL METHODS**

169 *In situ* bastnäsite U–Pb age determinations from eleven polished thin sections were
170 conducted using an Agilent 7900 quadrupole (Q)-ICP-MS coupled with a Resonetics

RESOlution S155 193 nm laser-ablation system at Guangzhou Institute of Geochemistry, Chinese Academy of Sciences (GIGCAS). Additional one bastnäsite sample (14MNP-40) was analyzed using an Agilent 7700 coupled with a Coherent 193 nm laser-ablation system at Institute of Geochemistry, Chinese Academy of Sciences. All analyses were undertaken with an energy density of 5 J/cm^2, beam diameter of 29/32 μm and a repetition rate of 5 Hz. Helium was used as a carrier gas to enhance the transportation efficiency of the ablated material. The U–Pb fractionation and instrumental mass discrimination of bastnäsite were normalized using the matrix-matched external bastnäsite standard K-9 (118 ± 1 Ma; Sal'nikova et al. 2010). Two reference analyses were measured after every five unknown bastnäsite sample spots. Each spot analysis consisted of 20 s background integration followed by 50 s sample data acquisition and then a 20 s delay to wash out the previous sample. Off-line data selection and integration were performed by using Iolite 3.64 software (Paton et al. 2011). Online Isoplot R (http://pieter-vermeesch.es.ucl.ac.uk/shiny/IsoplotRshiny/R/) was used to illustrate the U–Pb Tera-Wasserburg diagrams of bastnäsite (Vermeesch 2018).

The major oxide compositions of minerals were obtained using a JEOL JXA-8230 electron microprobe analyzer (EMPA) at GIGCAS. The analyses were carried out with an accelerating voltage of 15 kV, a beam current of 20 nA with diameter of 5 μm for apatite and 1 μm for clinopyroxene. Natural and synthetic minerals were used as standards. Matrix corrections were applied using a ZAF scheme. For the specific instrument test parameters and analysis protocols refer to Zeng et al. (2017). Trace element analyses were conducted with LA-ICPMS at GIGCAS. The measurements were made on thin sections using a laser beam diameter of 29 μm and an ablation rate of 5 Hz. The acquisition time for the background and sample signal was 20 s and 50 s,

196 respectively. NIST610 was used as external standard. Data reduction was made using
197 the CaO content obtained from EMPA as an internal standard. Integration of background
198 and analytical signals, and time-drift correction and quantitative calibration for trace
199 elements, were undertaken by using Iolite 3.64 software (Paton et al. 2011).

200 **RESULTS**

201 **U (Th)-Pb ages of bastnäsite**

202 The U (Th)-Pb isotopic data for bastnäsite are presented in Supplementary Table
203 1. Twelve samples and 243 analytical points were used for bastnäsite age
204 determination (Fig. 5). As the average value of the initial $^{207}Pb/^{206}Pb$ ratio of calcite in
205 Maoniuping deposit is 0.85 (Hou et al. 2015), we choose this as the initial value of
206 common Pb to anchor the bastnäsite age in Tera-Wasserburg diagrams. Three samples
207 of type-A bastnäsite (14MNP-40, 14MNP-44 and 14MNP-45) have U and Th
208 concentrations ranging from 2.98 to 69.3 ppm, and 8,030 to 51,360 ppm, respectively,
209 with Th/U ratios varying from 296 to 5,739. For type-A bastnäsite, we obtained an
210 acceptable lower intercept age of 28.2 ± 0.5 Ma (*n*=95, MSWD=5.10; Fig. 5a) on the
211 Tera-Wasserburg diagram. This is consistent with the weighted average $^{206}Pb/^{238}U$
212 age of 28.1 ± 0.5 Ma (*n*=95, MSWD=1.6; Fig. 5b) and $^{208}Pb/^{232}Th$ age of 28.2 ± 0.2
213 Ma (*n*=95, MSWD=2.8; Fig. 5b) after ^{207}Pb correction by using Pb isotopic
214 compositions from Stacey and Kramers (1975). Three samples of type-B bastnäsite
215 (MNPA-2, MNPB-2 and MNPC-1) have U and Th concentrations ranging from 16.9
216 to 79.1 ppm and 1,658 to 51,110 ppm, respectively, with Th/U ratios varying from
217 21.3 to 920. Forty three analyses of type-B bastnäsite form a well-fitting regression
218 line, yielding a lower intercept age of 27.8 ± 0.4 Ma (*n*=43, MSWD=0.73; Fig. 5c).
219 This is consistent (in error) with the weighted average $^{206}Pb/^{238}U$ age of 27.5 ± 0.6 Ma
220 (*n*=43, MSWD=1.2; Fig. 5d) and $^{208}Pb/^{232}Th$ age of 27.5 ± 0.2 Ma (*n*=43, MSWD=2.3;

Fig. 5d). Type-C bastnäsite from three samples (17MNP-1, 17MNP-6 and ZK311-12) has U and Th concentrations ranging from 23.8 to 120 ppm and 1,452 to 7,880 ppm, respectively, with Th/U ratios varying from 20.5 to 229. Fifty analyses yield an intercept age of 26.8 ± 0.7 Ma (*n*=50, MSWD=0.83; Fig. 5e), with a weighted average $^{206}Pb/^{238}U$ age of 26.3 ± 1.2 Ma (*n*=46, MSWD=1.2; Fig. 5f) and a weighted average $^{208}Pb/^{232}Th$ age of 26.8 ± 0.2 Ma (*n*=50, MSWD=2.2; Fig. 5f). Type-D bastnäsite from three samples (18MNP-16-1, ZK341-3-2 and ZK361-23) has U and Th contents ranging from 7.24 to 169 ppm and 2,611 to 45,630 ppm, respectively, with Th/U ratios varying from 59.9 to 1,067. Fifty-five analyses yield a lower intercept age of 25.8 ± 0.7 Ma (*n*=55, MSWD=1.7; Fig. 5g) and a weighted average $^{206}Pb/^{238}U$ age of 26.4 ± 2.2 Ma (*n*=42, MSWD=1.4; Fig. 5h). This is consistent with the weighted average $^{208}Pb/^{232}Th$ age of 25.8 ± 0.2 Ma (*n*=55, MSWD=1.9; Fig. 5h).

Compositions of bastnäsite, clinopyroxene and apatite

The compositional data for bastnäsite are listed in Supplementary Table 2 and summarized in Table 1. Compositionally, type-A bastnäsite shows some distinct features from the other three types of bastnäsite. It has relatively lower total REE (532,396–554,745 ppm) contents and $(La/Yb)_n$ (9,878–34,918) ratios than the other three types of bastnäsite (Table 1, Figs. 6a, 6c and 6d). Type-A bastnäsite is characterized by the relatively higher Sr (635–1,236 ppm) contents and δEu (0.67–0.98) value, as well as Th/U (296–5,739) ratios than other types of bastnäsite (Table 1, Figs. 6b, 6c and 6d).

The compositional data for clinopyroxene are presented in Supplementary Table 3 and summarized in Table 1. Clinopyroxene in the syenite is mostly aegirine ($Ae_{68-90}Di_{0-3}Hd_{10-30}$). In contrast, clinopyroxene in pegmatitic and carbonatite dikes is augite-aegirine with $Ae_{44-67}Di_{14-18}Hd_{17-41}$ and $Ae_{43-66}Di_{6-20}Hd_{21-38}$, respectively. Total

246 REE and Sr contents of clinopyroxene in syenite (1.01–4.44 ppm and 0.47–53.6 ppm,
247 respectively) are significantly lower than those in the pegmatitic (85.2–133 ppm and
248 87.9–240 ppm, respectively) and carbonatite dikes (85.7–170 ppm and 146–421 ppm,
249 respectively).

250 The compositional data for apatite are presented in Supplementary Table 4 and
251 summarized in Table 1. Apatite in syenite has a distinctively lower F (2.78–3.30
252 wt.%), Sr (2,913–7,331 ppm), and total REE (8,926–35,654 ppm) contents than
253 apatite in pegmatitic dikes (F=3.29–3.75 wt.%, Sr=4,833–10,630 ppm, total
254 REE=12,881–45,146 ppm) and apatite in carbonatite dikes (F=3.19–3.76 wt.%,
255 Sr=5,864–26,597 ppm, total REE=15,766–35,443 ppm) (Table 1, Figs. 8a, 8b and 8c).
256 Furthermore, apatite in syenite is also characterized by relatively higher CaO (51.9–
257 55.4 wt.%) contents, $(La/Yb)_n$ (16.1–194) and Ca/Sr (54.0–134) ratios than apatite in
258 pegmatitic dikes (CaO=51.2–53.5 wt.%, $(La/Yb)_n$=11.0–152, Ca/Sr=35.2–75.9) and
259 apatite in carbonatite dikes (CaO=49.8–53.6 wt.%, $(La/Yb)_n$=11.9–55.0, Ca/Sr=13.7–
260 62.4) (Table 1, Figs. 8b and 8d). Apatites from the syenite, pegmatitic and carbonatite
261 dikes are all fluorapatite, with no detectable Cl contents (Table 1).

262 **DISCUSSION AND CONCLUSION**

263 **Origin and age relationships of bastnäsite**

264 Bastnäsite is assumed usually to be a typical hydrothermal mineral, as it contains
265 volatile elements such as F and CO_2, which are generally enriched in late-stage
266 alkalis-enriched hydrothermal fluids (Bau and Dulski 1995; Agangi et al. 2010;
267 Migdisov and Williams-Jones 2014). In addition, REE, particularly LREE, are
268 strongly incompatible elements that are easily concentrated in such fluids (Michard
269 1989; Lottermoser 1992; Jaireth et al. 2014). For the Maoniuping deposit, previous
270 micro-thermometric results for the bastnäsite-hosted fluid inclusions have

homogenization temperatures of 137–270 °C (Niu et al. 1996, 1997; Xie et al. 2009, 2015; Liu et al. 2019a; Guo and Liu 2019). As a result of the previous studies, it was suggested that the large-scale precipitation of bastnäsite occurred in the late hydrothermal stage. However, in this investigation we identified a new paragenetic variety of bastnäsite of primary magmatic origin from the unaltered syenite, i.e. "type-A bastnäsite". This bastnäsite usually occurs as inclusions in orthoclase, indicating that it formed prior to orthoclase and might be synchronous with apatite or zircon (Fig. 3a). Isolated melt inclusions containing solid phase (>95 vol.%) are observed in type-A bastnäsite, indicating that they were formed in the magmatic stage (Fig. 3b). In contrast, other three paragenetic types of bastnäsite are interpreted to be of hydrothermal origin, on the basis of the occurrence of primary fluid inclusions and previous micro-thermometry investigations. The macro-crystalline bastnäsite (type-B) in the pegmatitic dikes is euhedral and tabular, and is host to a large variety of fluid inclusions (Figs. 3c and 3d). The bastnäsite grains in the veinlets of the altered syenite (type-C) and carbonatite dikes (type-D) are mostly anhedral with abundant vapor-liquid fluid inclusions (Figs. 3f and 3h), indicating a hydrothermal origin.

The bastnäsite U–Pb data are highly reliable, even with the variable amounts of common lead (Fig. 5), and indicate a continuous evolution of bastnäsite crystallization from 28.2 Ma to 25.8 Ma. Compared with previous geochronological data, our bastnäsite U–Pb data have a much higher accuracy and a more reliable age for the REE mineralization of the Maoniuping deposit. In earlier investigations mineralization ages of 31–40 Ma were determined using mica and amphibole K-Ar geochronology, which highlighted the presence of excess Ar (Yuan et al. 1995). With the refinement of analytical techniques, recent Ar-Ar methods yield ages of 25–30 Ma (Liu and Hou 2017; Liu et al. 2019a). Zircon from the syenite yields SHRIMP U–Pb

296 ages of 21.3–22.8 Ma (Liu et al. 2015) and 26.6 Ma by SIMS (Ling et al. 2016),
297 indicating the possible loss of radiogenic Pb in zircon during late hydrothermal
298 alteration (Liu et al. 2019b). A bastnäsite sample from an unknown location or
299 genesis yielded a LA-ICPMS U–Pb age of 31.9±3.9 Ma (Yang et al. 2014b) and a
300 SIMS Th–Pb age of 25.7±0.2 Ma (Ling et al. 2016).

301 These data from previous studies required an integrated understanding of the
302 evolution of the alkaline complex. Our new data show that the primary bastnäsite in
303 syenite formed earlier than that in the other three paragenetic types of hydrothermal
304 bastnäsite. Subsequently, crystallization of abundant REE minerals in the pegmatitic
305 dikes, secondary veinlets in the syenite and the carbonatite dikes occurred during a
306 late hydrothermal stage. This evolutionary relationship is similar to that proposed for
307 the Mountain Pass REE deposit (e.g., Poletti et al. 2016). Therefore, the primary and
308 hydrothermal bastnäsite in the Maoniuping deposit indicates continuous REE
309 mineralization during the magmatic and hydrothermal evolution of the
310 syenite-carbonatite complex.

311 **Genesis and implications of clinopyroxene and apatite**

312 Clinopyroxene is a ubiquitous mineral in alkaline complexes, and usually
313 displays extensive compositional variation with the potential to incorporate many
314 geochemically-relevant trace elements (e.g., Marks et al. 2004). In the Maoniuping
315 deposit, clinopyroxenes in the pegmatitic and carbonatite dikes show similar REE
316 distribution patterns to those of typical magmatic clinopyroxene from worldwide
317 carbonatites (e.g., Reguir et al. 2012; Fig. 7a). In contrast, clinopyroxene in the
318 syenite has a similar REE distribution pattern to that of the Strange Lake peralkaline
319 granite (Vasyukova and Williams-Jones 2018), with notably lower REE contents (Fig.
320 7a). Clinopyroxene shows two distinctive evolutionary trends in composition (Figs. 7c

and 7d). Previous studies have determined that the evolutionary trend of clinopyroxene compositions in alkaline complexes is usually from the Ca- and Mg-rich pyroxene (diopside) towards the Na- and Fe-rich end-member (aegirine) as the magmatic evolutions (e.g., Larsen 1976; Mitchell and Platt 1982; Markl et al. 2001; Coulson 2003; Marks et al. 2008). Alternatively, the trend can be from diopside via hedenbergite to aegirine at relatively low oxygen fugacity (e.g., Mitchell and Platt 1978; Markl et al. 2001). At Maoniuping, clinopyroxene in the syenite is mostly aegirine ($Ae_{68–90}Hd_{10–30}Di_{0–3}$), whereas, clinopyroxene in the pegmatite ($Ae_{44–67}Hd_{17–41}Di_{14–17}$) and carbonatite ($Ae_{43–66}Hd_{21–38}Di_{6–20}$) is augite-aegirine (Table 1, Figs. 7c and 7d). These data suggest that the calcic-sodic series of clinopyroxene in the pegmatitic and carbonatite dikes was probably formed from the same magma system, and is genetically different to the sodic series in the syenite. Therefore, the evolution of clinopyroxene suggests that the pegmatitic and carbonatite dikes might result from segregation from a REE- and volatile-rich melt (i.e., initial carbonatitic melt), rather than residual melt/fluid origins from the syenitic magma.

Apatite is predominantly fluorapatite with compositional characteristics of magmatic origin, including enrichment of REE and Sr (e.g., Chakhmouradian et al. 2017). Compared to apatite in the syenite, apatites in the pegmatitic and carbonatite dikes generally have higher F (3.19–3.76 wt.%), Sr (4,833–26,597 ppm), total REE (12,881–45,146 ppm) and lower Ca/Sr and $(La/Yb)_n$ ratios (Table 1; Fig. 8). These data are consistent with petrological observations that the pegmatitic and carbonatite dikes are enriched in incompatible and volatile components (e.g., REE, Sr, F and CO_2). The differences in apatite composition between the syenite, pegmatitic and carbonatite dikes give additional support to the hypothesis that the pegmatitic dikes are genetically related to the carbonatite melt/fluid rather than the syenite melt.

Genetic model

On the basis of our bastnäsite U–Pb data and the compositions of clinopyroxene and apatite, four continuous stages of REE mineralization have been recognized in this study. At ca. 28.2 Ma, the syenite first intruded into the rhyolite and Mesozoic alkaline granite, forming the ore-barren syenite plutons with minor primary bastnäsite. Subsequently, the pegmatitic dikes were intruded into the syenite and the nearby Mesozoic alkaline granite at ca. 27.8 Ma. These hydrous melts/fluids were oversaturated with REE and were saline- and sulfate-enriched, resulting in large-scale REE precipitation. Subsequently, intensive fluid interaction occurred within the previously emplaced syenite, forming the widespread veinlets at 26.8 Ma. Finally, the carbonatite was intruded as dikes or stocks at ca. 25.8 Ma. This paragenetic sequence is supported by the four generations of bastnäsite and the U–Pb geochronology. During these generations, the early bastnäsite was recognized as being of magmatic origin, whereas the three later bastnäsite are of hydrothermal origin. The compositions of clinopyroxene and apatite provide additional evidence for the genetic relationship between the pegmatitic and carbonatite dikes. Such magmatic and hydrothermal evolution highlights multi-stage crystallization of REE mineral to form the Maoniuping deposit. Our new bastnäsite U–Pb data suggest that this evolution probably spanned over at least 2.5 Ma.

IMPLICATIONS

This study has concluded that bastnäsite can be used as a potential indicator of magmatic-hydrothermal evolution and associated REE mineralization processes. In the giant Maoniuping deposit, bastnäsite is the dominant economic mineral, occurring as four paragenetic types in the syenite–carbonatite complex. Combined with the paragenetic and compositional variations, we inferred that type-A bastnäsite is of

primary magmatic origin, whereas the other three types have characteristics of hydrothermal origins. *In situ* LA-ICPMS U (Th)–Pb geochronology of the four types of bastnäsite indicates a prolonged multi-stage REE mineralization during the evolution of Maoniuping alkaline complex. Compositional variations of clinopyroxene and apatite favor an explanation of that the pegmatitic melt should be directly separated from the initial carbonatitic melt rather than the syenitic magma. This work shows that bastnäsite geochemistry could be a powerful indicator mineral of magmatic-hydrothermal evolution and REE mineralization of alkaline-carbonatite complexes.

ACKNOWLEDGEMENTS

This work was supported by the National Key R&D Program of China (No. 2017YFC0602301), National Natural Science Foundation of China (No. 41930424), Youth Innovation Promotion Association CAS (2017405) and Science and Technology Planning of Guangdong Province, China (2020B1212060055). Prof. Yuling Xie and three anonymous referees are highly appreciated for their constructive suggestions and comments. This is contribution No. IS-2951 from GIGCAS.

REFERENCES CITED

109 Geological Brigade of Sichuan Bureau of Geology and Mineral Resource (2010) Exploration report of Maoniuping REE deposit in Mianning, Sichuan Province.

Agangi, A., Kamenetsky, V.S., and McPhie, J. (2010) The role of fluorine in the concentration and transport of lithophile trace elements in felsic magmas: insights from the Gawler Range Volcanics, South Australia. Chemical Geology, 273, 314–325.

Bau, M., and Dulski, P. (1995) Comparative study of yttrium and rare-earth element behaviours in fluorine-rich hydrothermal fluids. Contributions to Mineralogy and Petrology, 119, 213–223.

Broom-Fendley, S., Wall, F., Spiro, B., and Ullmann, C.V. (2017) Deducing the source and composition of rare earth mineralising fluids in carbonatites: insights from isotopic (C, O, $^{87}Sr/^{86}Sr$) data from Kangankunde, Malawi. Contributions to Mineralogy and Petrology, 172, 1–18.

Castor, S.B. (2008) The Mountain Pass rare-earth carbonatite and associated ultrapotassic rocks, California. Canadian Mineralogist, 46, 779–806.

Chakhmouradian, A.R., Reguir, E.P., Zaitsev, A.N., Couëslan, C., Xu, C., Kynický, J., Mumin, A.H., and Yang, P. (2017) Apatite in carbonatitic rocks: compositional variation, zoning, element partitioning and petrogenetic significance. Lithos, 274–275, 188–213.

Chakhmouradian, A.R., and Wall, F. (2012) Rare earth elements: minerals, mines, magnets (and more). Elements, 8, 333–340.

Coulson, I.M. (2003) Evolution of the North Qôroq centre nepheline syenites, South

Greenland: alkali-mafic silicates and the role of metasomatism. Mineralogical Magazine, 67, 873–892.

Feng, M., Song, W., Kynicky, J., Smith, M., Cox, C., Kotlanova, M., Brtnicky, M., Fu, W., and Wei, C. (2020) Primary rare earth element enrichment in carbonatites: Evidence from melt inclusions in Ulgii Khiid carbonatite, Mongolia. Ore Geology Reviews, 117, 103294.

Giebel, R.J., Gauert, C.D.K., Marks, M.A.W., Costin, G., and Markl, G. (2017) Multi-stage formation of REE minerals in the Palabora Carbonatite Complex, South Africa. American Mineralogist, 102, 1218–1233.

Guo, D.X., and Liu, Y. (2019) Occurrence and geochemistry of bastnäsite in carbonatite-related REE deposits, Mianning–Dechang REE belt, Sichuan Province, SW China. Ore Geology Reviews, 107, 266–282.

Guo, Z.F., Hertogen, J.A.N., Liu, J.Q., Pasteels, P., Boven, A., Punzalan, L.E.A., He, H.Y., Luo, X.J., and Zhang, W.H. (2005) Potassic magmatism in western Sichuan and Yunnan Provinces, SE Tibet, China: petrological and geochemical constraints on petrogenesis. Journal of Petrology, 46, 33–78.

Gysi, A.P., and Williams-Jones, A.E. (2015) The thermodynamic properties of bastnäsite-(Ce) and parisite-(Ce). Chemical Geology, 392, 87–101.

Hou, Z.Q., and Cook, N.J. (2009) Metallogenesis of the Tibetan collisional orogen: a review and introduction to the special issue. Ore Geology Reviews, 36, 2–24.

Hou, Z.Q., Liu, Y., Tian, S.H., Yang, Z.M., and Xie, Y.L. (2015) Formation of carbonatite-related giant rare-earth-element deposits by the recycling of marine sediments. Scientific Reports, 5, 1–10.

433 Hou, Z.Q., Ma, H.W., Khin, Z., Zhang, Y.Q., Wang, M.J., Wang, Z., Pan, G.T., and Tang,
434 R.L. (2003) The Himalayan Yulong porphyry copper belt: product of large-scale
435 strike-slip faulting in eastern Tibet. Economic Geology, 98, 125–145.
436 Jaireth, S., Hoatson, D.M., and Miezitis, Y. (2014) Geological setting and resources of the
437 major rare-earth-element deposits in Australia. Ore Geology Reviews, 62, 72–128.
438 Larsen, L.M. (1976) Clinopyroxenes and coexisting mafic minerals from the alkaline
439 Ilímaussaq intrusion, south Greenland. Journal of Petrology, 17, 258–290.
440 Ling, X.X., Li, Q.L., Liu, Y., Yang, Y.H., Liu, Y., Tang, G.Q., and Li, X.H. (2016) In situ
441 SIMS Th–Pb dating of bastnaesite: constraint on the mineralization time of the
442 Himalayan Mianning–Dechang rare earth element deposits. Journal of Analytical
443 Atomic Spectrometry, 31, 1680–1687.
444 Liu, Y., Chakhmouradian, A.R., Hou, Z.Q., Song, W.L., and Kynický, J. (2019a)
445 Development of REE mineralization in the giant Maoniuping deposit (Sichuan,
446 China): insights from mineralogy, fluid inclusions, and trace-element
447 geochemistry. Mineralium Deposita, 54, 701–718.
448 Liu, Y., and Hou, Z.Q. (2017) A synthesis of mineralization styles with an integrated
449 genetic model of carbonatite-syenite-hosted REE deposits in the Cenozoic
450 Mianning-Dechang REE metallogenic belt, the eastern Tibetan Plateau,
451 southwestern China. Journal of Asian Earth Sciences, 137, 35–79.
452 Liu, Y., Hou, Z.Q., Tian, S.H., Zhang, Q.C., Zhu, Z.M., and Liu, J.H. (2015) Zircon U–Pb
453 ages of the Mianning–Dechang syenites, Sichuan Province, southwestern China:
454 constraints on the giant REE mineralization belt and its regional geological setting.
455 Ore Geology Reviews, 64, 554–568.

Liu, Y., Hou, Z.Q., Zhang, R.Q., Wang, P., Gao, J.F., and Raschke, M.B. (2019b) Zircon alteration as a proxy for rare earth element mineralization processes in carbonatite-nordmarkite complexes of the Mianning-Dechang rare earth element belt, China. Economic Geology, 114, 719–744.

Lottermoser, B.G. (1992) Rare earth elements and hydrothermal ore formation processes. Ore Geology Reviews, 7, 25–41.

Mann, U., Marks, M.A.W., and Markl, G. (2006) Influence of oxygen fugacity on mineral compositions in peralkaline melts: the Katzenbuckel volcano, southwest Germany. Lithos, 91, 262–285.

Mariano, A.N. (1989) Nature of economic mineralization in carbonatites and related rocks. In K. Bell, Eds., Carbonatites: Genesis and Evolution, p. 149–176. Unwin Hyman, London.

Markl, G., Marks, M., Schwinn, G., and Sommer, H. (2001) Phase equilibrium constraints on intensive crystallization parameters of the Ilímaussaq complex, South Greenland. Journal of Petrology, 42, 2231–2257.

Marks, M., Halama, R., Wenzel, T., and Markl, G. (2004) Trace element variations in clinopyroxene and amphibole from alkaline to peralkaline syenites and granites: implications for mineral-melt trace-element partitioning. Chemical Geology, 211, 185–215.

Marks, M.A.W., Schilling, J., Coulson, I.M., Wenzel, T., and Markl, G. (2008) The alkaline-peralkaline Tamazeght complex, High Atlas Mountains, Morocco: mineral chemistry and petrological constraints for derivation from a compositionally heterogeneous mantle source. Journal of Petrology, 49, 1097–

1131.

McDonough, W.F., and Sun, S.S. (1995) The composition of the earth. Chemical Geology, 120, 223–253.

Michard, A. (1989) Rare earth element systematics in hydrothermal fluids. Geochimica et Cosmochimica Acta, 53, 745–750.

Migdisov, A.A., and Williams-Jones, A. (2014) Hydrothermal transport and deposition of the rare earth elements by fluorine-bearing aqueous liquids. Mineralium Deposita, 49, 987–997.

Mitchell, R.H. (2005) Carbonatites and carbonatites and carbonatites. Canadian Mineralogist, 43, 2049–2068.

Mitchell, R.H., and Platt, R.G. (1978) Mafic mineralogy of ferroaugite syenite from the Coldwell alkaline complex, ontario, Canada. Journal of Petrology, 19, 627–651.

Mitchell, R.H., and Platt, R.G. (1982) Mineralogy and petrology of nepheline syenites from the Coldwell alkaline complex, Ontario, Canada. Journal of Petrology, 23, 186–214.

Niu, H.C., and Lin, C.X. (1994) The genesis of the Mianning REE deposit, Sichuan Province. Mineral Deposits, 13, 345–353 (in Chinese with English abstract).

Niu, H.C., Shan, Q., and Lin, M.Q. (1996) A study on inclusions in minerals from Mianning REE deposit in Sichuan Province. Geochimica, 25, 559–567 (in Chinese with English abstract).

Niu, H.C., Shan, Q., and Lin, M.Q. (1997) Fluid-melt and fluid inclusions in Mianning REE deposit, Sichuan, Southwest China. Chinese Journal of Geochemistry, 16, 256–262.

Paton, C., Hellstrom, J., Paul, B., Woodhead, J., and Hergt, J. (2011) Iolite: freeware for the visualisation and processing of mass spectrometric data. Journal of Analytical Atomic Spectrometry, 26, 2508–2518.

Poletti, J.E., Cottle, J.M., Hagen-Peter, G.A., and Lackey, J.S. (2016) Petrochronological constraints on the origin of the Mountain Pass ultrapotassic and carbonatite intrusive suite, California. Journal of Petrology, 57, 1555–1598.

Pu, G.P. (1993) A discussion on metallogenetic model and prospecting targets for Maoniuping ore deposit of rare-earth elements. Acta Geologica Sichuan, 13, 46–57 (in Chinese with English abstract).

Reguir, E.P., Chakhmouradian, A.R., Pisiak, L., Halden, N.M., Yang, P., Xu, C., Kynický, J., and Couëslan, C.G. (2012) Trace-element composition and zoning in clinopyroxene- and amphibole-group minerals: implications for element partitioning and evolution of carbonatites. Lithos, 128–131, 27–45.

Sal'nikova, E.B., Yakovleva, S.Z., Nikiforov, A.V., Kotov, A.B., Yarmolyuk, V.V., Anisimova, I.V., Sugorakova, A.M., and Plotkina, Y.V. (2010) Bastnaesite: a promising U-Pb geochronological tool. Doklady Earth Sciences, 430, 134–136.

Smith, M.P., Henderson, P., and Campbell, L.S. (2000) Fractionation of the REE during hydrothermal processes: constraints from the Bayan Obo Fe-REE-Nb deposit, Inner Mongolia, China. Geochimica et Cosmochimica Acta, 64, 3141–3160.

Stacey, J.S., and Kramers, J.D. (1975) Approximation of terrestrial lead isotope evolution by a two-stage model. Earth and Planetary Science Letters, 26, 207–221.

Vasyukova, O.V., and Williams-Jones, A.E. (2018) Direct measurement of metal concentrations in fluid inclusions, a tale of hydrothermal alteration and REE ore

525 formation from Strange Lake, Canada. Chemical Geology, 483, 385–396.
526 Vermeesch, P. (2018) IsoplotR: a free and open toolbox for geochronology. Geoscience
527 Frontiers, 9, 1479–1493.
528 Vuorinen, J.H., Halenius, U., Whitehouse, M.J., Mansfeld, J., and Skelton, A.D.L. (2005)
529 Compositional variations (major and trace elements) of clinopyroxene and
530 Ti-andradite from pyroxenite, ijolite and nepheline syenite, Alnö Island, Sweden.
531 Lithos, 81, 55–77.
532 Weng, Z.H., Jowitt, S.M., Mudd, G.M., and Haque, N. (2015) A detailed assessment of
533 global rare earth element resources: opportunities and challenges. Economic
534 Geology, 110, 1925–1952.
535 Williams-Jones, A.E., Samson, I.M., and Olivo, G.R. (2000) The genesis of hydrothermal
536 fluorite-REE deposits in the Gallinas Mountains, New Mexico. Economic
537 Geology, 95, 327–341.
538 Xie, Y.L., Hou, Z.Q., Goldfarb, R., Guo, X., and Wang, L. (2016) Rare earth element
539 deposits in China. Reviews in Economic Geology, 18, 115–136.
540 Xie, Y.L., Hou, Z.Q., Yin, S.P., Dominy, S.C., Xu, J.H., Tian, S.H., and Xu, W.Y. (2009)
541 Continuous carbonatitic melt–fluid evolution of a REE mineralization system:
542 evidence from inclusions in the Maoniuping REE deposit, Western Sichuan, China.
543 Ore Geology Reviews, 36, 90–105.
544 Xie, Y.L., Li, Y.X., Hou, Z.Q., Cooke, D.R., Danyushevsky, L., Dominy, S.C., and Yin,
545 S.P. (2015) A model for carbonatite hosted REE mineralisation–the Mianning–
546 Dechang REE belt, Western Sichuan Province, China. Ore Geology Reviews, 70,
547 595–612.

548 Yang, W.B., Niu, H.C., Shan, Q., Sun, W.D., Zhang, H., Li, N.B., Jiang, Y.H., and Yu,
549 X.Y. (2014a) Geochemistry of magmatic and hydrothermal zircon from the highly
550 evolved Baerzhe alkaline granite: implications for Zr–REE–Nb mineralization.
551 Mineralium Deposita, 49, 451–470.
552 Yang, Y.H., Wu, F.Y., Li, Y., Yang, J.H., Xie, L.W., Liu, Y., Zhang, Y.B., and Huang, C.
553 (2014b) In situ U–Pb dating of bastnaesite by LA-ICP-MS. Journal of Analytical
554 Atomic Spectrometry, 29, 1017–1023.
555 Yin, A., and Harrison, T.M. (2000) Geologic evolution of the Himalayan-Tibetan orogen.
556 Annual Review of Earth and Planetary Sciences, 28, 211–280.
557 Yuan, Z.X., Shi, Z.M., Bai, G., Wu, C.Y., Chi, R.A., and Li, X.Y. (1995) The Maoniuping
558 rare earth ore deposit, Mianning county, Sichuan Province, 150 p. Seismological
559 Publishing House, Beijing (in Chinese).
560 Zaitsev, A.N., Terry Williams, C., Jeffries, T.E., Strekopytov, S., Moutte, J.,
561 Ivashchenkova, O.V., Spratt, J., Petrov, S.V., Wall, F., Seltmann, R., and Borozdin,
562 A.P. (2014) Rare earth elements in phoscorites and carbonatites of the Devonian
563 Kola Alkaline Province, Russia: Examples from Kovdor, Khibina, Vuoriyarvi and
564 Turiy Mys complexes. Ore Geology Reviews, 61, 204–225.
565 Zeng, L.J., Niu, H.C., Bao, Z.W., and Yang, W.B. (2017) Chemical lattice expansion of
566 natural zircon during the magmatic-hydrothermal evolution of A-type granite.
567 American Mineralogist, 102, 655–665.
568
569
570

FIGURE CAPTIONS

Figure 1. Position and geological map of the Maoniuping gaint REE deposit. (**a**) Simplified tectonic map of the Himalayan–Tibetan orogeny shows that the Maoniuping REE deposit is located in the east of Tibetan plateau and affected by post-collision event of India-Asia continent. (**b**) Simplified geological map of the Maoniuping REE deposit (modified after Yuan et al. 1995). Dagudao and Guangtoushan are the two open pits currently in production.

Figure 2. Representative hand specimens of rock and ore sample in the Maoniuping deposit. (**a**) Unaltered syenite with primary (type-A) bastnäsite. (**b**) A representative sample of pegmatite with hydrothermal (Type-B) bastnäsite. (**c**) A secondary veinlet with hydrothermal (type-C) bastnäsite is hosted in the altered syenite. (**d**) A representative sample of carbonatite with hydrothermal (Type-D) bastnäsite. Abbreviations: Bast=bastnäsite, Afs=alkali-feldspar, Cal=calcite, Brt=barite, Qz=quartz, Cpx=clinopyroxene, Fl=fluorite.

Figure 3. Representative microphotographs of four types of bastnäsite in the Maoniuping deposit. (**a**) Primary euhedral, nearly hexagonal bastnäsite (type-A) in syenite occurs within euhedral orthoclase (Or) and (**b**) nearly rounded melt inclusion can be found in this type of bastnäsite. (**c**) Euhedral to subhedral bastnäsite (type-B) associated with barite in pegmatite occurs as a thick tabular megacryst and (**d**) hosts liquid-rich fluid inclusions. (**e**) Euhedral to anhedral veinlet-disseminated bastnäsite (type-C) hosts in altered syenite and (**f**) contains variably shaped fluid inclusions. (**g**) Anhedral to subhedral bastnäsite (type-D) interstitial to calcite in carbonatite and (**h**) hosts liquid-rich fluid inclusions. V = vapour phase, L =

595 liquid phase. Mineral abbreviations are shown in Fig. 2.

596

597 **Figure 4.** Representative BSE images of clinopyroxene (Cpx) and apatite (Ap) in the
598 Maoniuping deposit. (**a**) Euhedral clinopyroxene occurs as prismatic crystal in syenite. (**b**)
599 Euhedral clinopyroxene megacryst in pegmatite is closely associated with barite, fluorite
600 and minor calcite. (**c**) Euhedral clinopyroxene intergrowth with euhedral calcite in
601 carbonatite. (**d**) Euhedral apatite occurs as prismatic or hexagonal crystal in syenite. (**e**)
602 Euhedral and prismatic apatite hosted in clinopyroxene megacrystal from the pegmatitic
603 dikes. (**f**) Euhedral apatite hosted in calcite megacrystal from the carbonatite dikes. Mineral
604 abbreviations are shown in Fig. 2.

605

606 **Figure 5.** Tera–Wasserburg concordia diagrams and weighted average $^{206}Pb/^{238}U$ and
607 $^{208}Pb/^{232}Th$ ages of four types of bastnäsite from the Maoniuping REE deposit. (**a** and **b**)
608 Three samples of type-A bastnäsite yield a lower interpreted age of 28.2±0.5 Ma and the
609 weighted average $^{206}Pb/^{238}U$ age of 28.1±0.5 Ma and $^{208}Pb/^{232}Th$ age of 28.2±0.2 Ma. (**c** and
610 **d**) Three samples of type-B bastnäsite yield a lower interpreted age of 27.8±0.4 Ma and the
611 weighted average $^{206}Pb/^{238}U$ age of 27.5±0.6 Ma and $^{208}Pb/^{232}Th$ age of 27.5±0.2 Ma. (**e** and **f**)
612 Three samples of type-C bastnäsite yield a lower interpreted age of 26.8±0.7 Ma and the
613 weighted average $^{206}Pb/^{238}U$ age of 26.3±1.2 Ma and $^{208}Pb/^{232}Th$ age of 26.8±0.2 Ma. And (**g**
614 and **h**) three samples of type-D bastnäsite yield a lower interpreted age of 25.8±0.7 Ma and
615 the weighted average $^{206}Pb/^{238}U$ age of 26.4±2.2 Ma and $^{208}Pb/^{232}Th$ age of 25.8±0.2 Ma. In
616 the Tera–Wasserburg concordia diagrams, the lower intercept ages were calculated by
617 anchored the initial common Pb value at $^{207}Pb/^{206}Pb=0.85$. The weighted average $^{206}Pb/^{238}U$

618 and $^{208}Pb/^{232}Th$ ages were recalibrated by a ^{207}Pb-based corrected method.

619

620 **Figure 6.** Chemical distribution and variation diagrams of four types of bastnäsite (Bast)
621 from the Maoniuping deposit. (**a**) Chondrite-normalized REE patterns for four types of
622 bastnäsite. Chondrite values are taken from McDonough and Sun (1995). (**b**) Th versus U
623 diagram. (**c**) Sr versus total REE diagram. (**d**) δEu versus $(La/Yb)_n$ diagram.

624

625 **Figure 7.** Chemical distribution and variation diagrams of clinopyroxene (Cpx) from the
626 Maoniuping deposit. (**a**) Chondrite-normalized REE patterns for clinopyroxene. The shaded
627 region is the REE pattern of typical magmatic clinopyroxene from Alnö, Oka, Eden Lake and
628 Oz.Varaka carbonatite (Reguir et al. 2012) and the gray dotted line is the late aegirine from
629 the Strange Lake deposit in Canada (Vasyukova and Williams-Jones 2018). Chondrite values
630 are taken from McDonough and Sun (1995). (**b**) Plot of Sr versus total REE. (**c**) Plot of Q
631 versus J. Quad (quadrilateral) represents Mg-Fe-Ca pyroxene group, Ca-Na represents
632 Ca-Na pyroxene group and Na represents Na pyroxene group. (**d**) The variation in the Di
633 (diopside, $CaMgSi_2O_6$)-Hd (hedenbergite, $CaFe^{2+}Si_2O_6$)-Ae (aegirine, $NaFe^{3+}Si_2O_6$)
634 projection for clinopyroxene from the syenite, pegmatitic and carbonatite dikes. "A"
635 represents an extreme pyroxene evolutionary path of from diopside to aegirine (e.g.,
636 Katzenbuckel alkaline complex, SW Germany, Mann et al. 2006), "B" represents an
637 extreme pyroxene evolutionary path from diopside through hedenbergite, then to aegirine
638 (e.g., Ilímaussaq alkaline complex, South Greenland, Markl et al. 2001) and "C" represents
639 an intermediate evolutionary path (e.g., Alnö alkaline complex, Sweden, Vuorinen et al.
640 2005).

641

642 **Figure 8.** Chemical distribution and variation diagrams of apatite (Ap) from the Maoniuping
643 deposit. (**a**) Chondrite-normalized REE patterns for apatite. Chondrite values are taken from
644 McDonough and Sun (1995). The shaded region is the REE pattern of typical magmatic
645 apatite from Aley alkaline complex (Chakhmouradian et al. 2017). (**b**) Plots of F versus CaO,
646 (**c**) total REE versus Sr, and (**d**) Ca/Sr versus $(La/Yb)_n$ for apatite from the syenite, pegmatitic
647 and carbonatite dikes. The black dotted lines show that the apatite from the pegmatitic and
648 carbonatite dikes is obviously different from the apatite from the syenite, indicating that the
649 pegmatitic and the carbonatite dikes have obvious affinity.

650

651 **Figure 9.** Schematic genetic model of the Maoniuping giant REE deposit. The crystallization
652 of primary bastnäsite (type-A) in syenite represents the beginning of REE mineralization
653 (~28.2 Ma). The formation of hydrothermal bastnäsite (type-B) in pegmatitic dikes represents
654 REE mineralization associated with sulfate melt (~27.8 Ma). The formation of hydrothermal
655 bastnäsite veinlets (type-C) in syenite represents REE mineralization associated with syenite
656 (~26.8 Ma). The formation of hydrothermal bastnäsite (type-D) in carbonatite represents
657 REE mineralization associated with carbonate melt (~25.8 Ma). Mineral abbreviations are
658 shown in Fig. 2.

This is the peer-reviewed, final accepted version for American Mineralogist, published by the Mineralogical Society of America.
The published version is subject to change. Cite as Authors (Year) Title. American Mineralogist, in press.
DOI: https://doi.org/10.2138/am-2021-7778. http://www.minsocam.org/

659 **Table 1.** Geochemical variations of bastnäsite, clinopyroxene and apatite with different
660 parageneses in the Maoniuping complex.

Bastnäsite	In syenite (Type-A, n=13)	In pegmatite (Type-B, n=24)	In veinlet (Type-C, n=15)	In carbonatite (Type-D, n=31)
U (ppm)	2.98–69.3	16.9–79.1	23.8–120	7.24–169
Th (ppm)	8,030–51,360	1,658–51,110	1,452–7,880	2,611–45,630
Th/U	296–5,739	21.3–920	20.5–229	59.9–1,067
Sr (ppm)	635–1,236	312–489	306–644	284–624
REE (ppm)	532,396–554,745	602,924–605,036	613,459–615,898	595,881–605,909
$(La/Yb)_n$	9,878–34,918	33,763–81,059	45,729–249,521	29,272–132,867
δEu	0.67–0.98	0.56–0.62	0.52–0.66	0.42–0.62
Age (Ma)	28.2 ± 0.5 (n=95)	27.8 ± 0.4 (n=43)	26.8 ± 0.7 (n=50)	25.8 ± 0.7 (n=55)
Clinopyroxene	In syenite (n=18)	In pegmatite (n=19)		In carbonatite (n=11)
Ae (%)	67.6–89.7	44.1–66.5	/	43.3–65.7
Di (%)	0.01–2.61	14.4–17.5	/	6.38–19.9
Hd (%)	9.60–29.8	16.9–41.0	/	20.8–37.7
REE (ppm)	1.01–4.44	85.2–133	/	85.7–170
Sr (ppm)	0.47–53.6	87.9–240	/	146–421
Apatite	In syenite (n=17)	In pegmatite (n=15)		In carbonatite (n=15)
CaO (wt.%)	51.9–55.4	51.2–53.5	/	49.8–53.6
F (wt.%)	2.78–3.30	3.29–3.75	/	3.19–3.76
Cl (wt.%)	bdl	bdl	/	bdl
Sr (ppm)	2,913–7,331	4,833–10,630	/	5,864–26,597
REE (ppm)	8,926–35,654	12,881–45,146	/	15,766–35,443
$(La/Yb)_n$	16.1–194	11.0–152	/	11.9–55.0
Ca/Sr	54.0–134	35.2–75.9	/	13.7–62.4

661 Notes: "bdl" means below detection limit; "/" means no data available

Figure 1

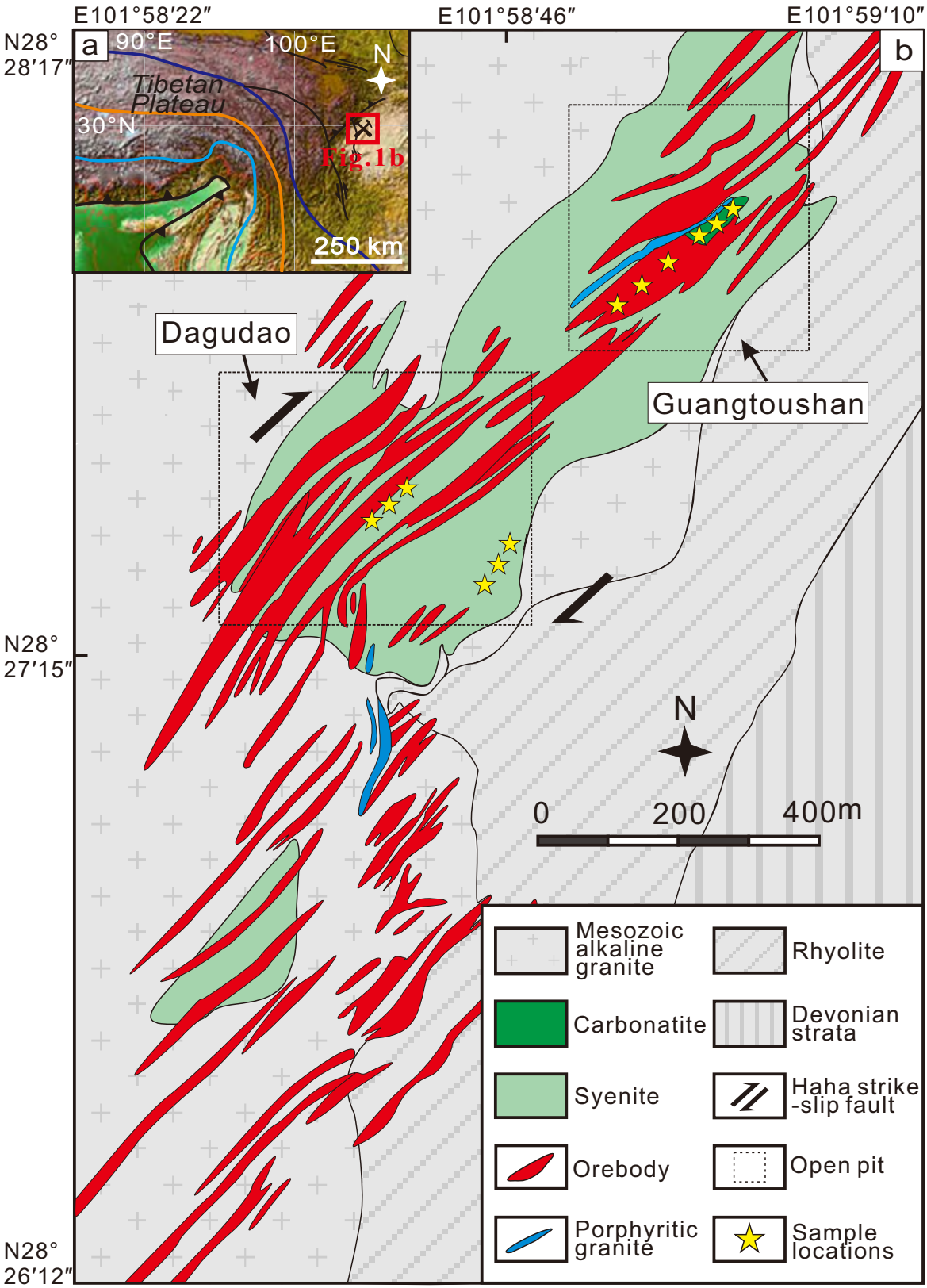

This is the peer-reviewed, final accepted version for American Mineralogist, published by the Mineralogical Society of America.
The published version is subject to change. Cite as Authors (Year) Title. American Mineralogist, in press.
DOI: https://doi.org/10.2138/am-2021-7778. http://www.minsocam.org/

Figure 2

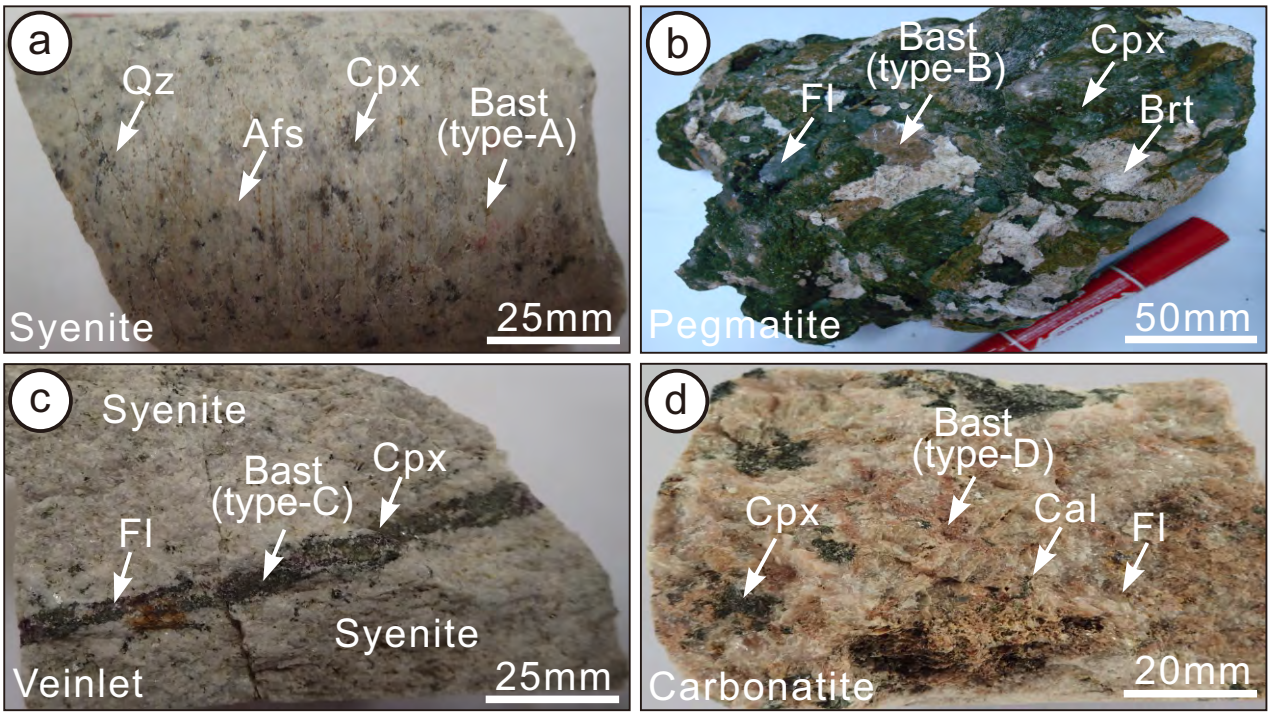

Figure 3

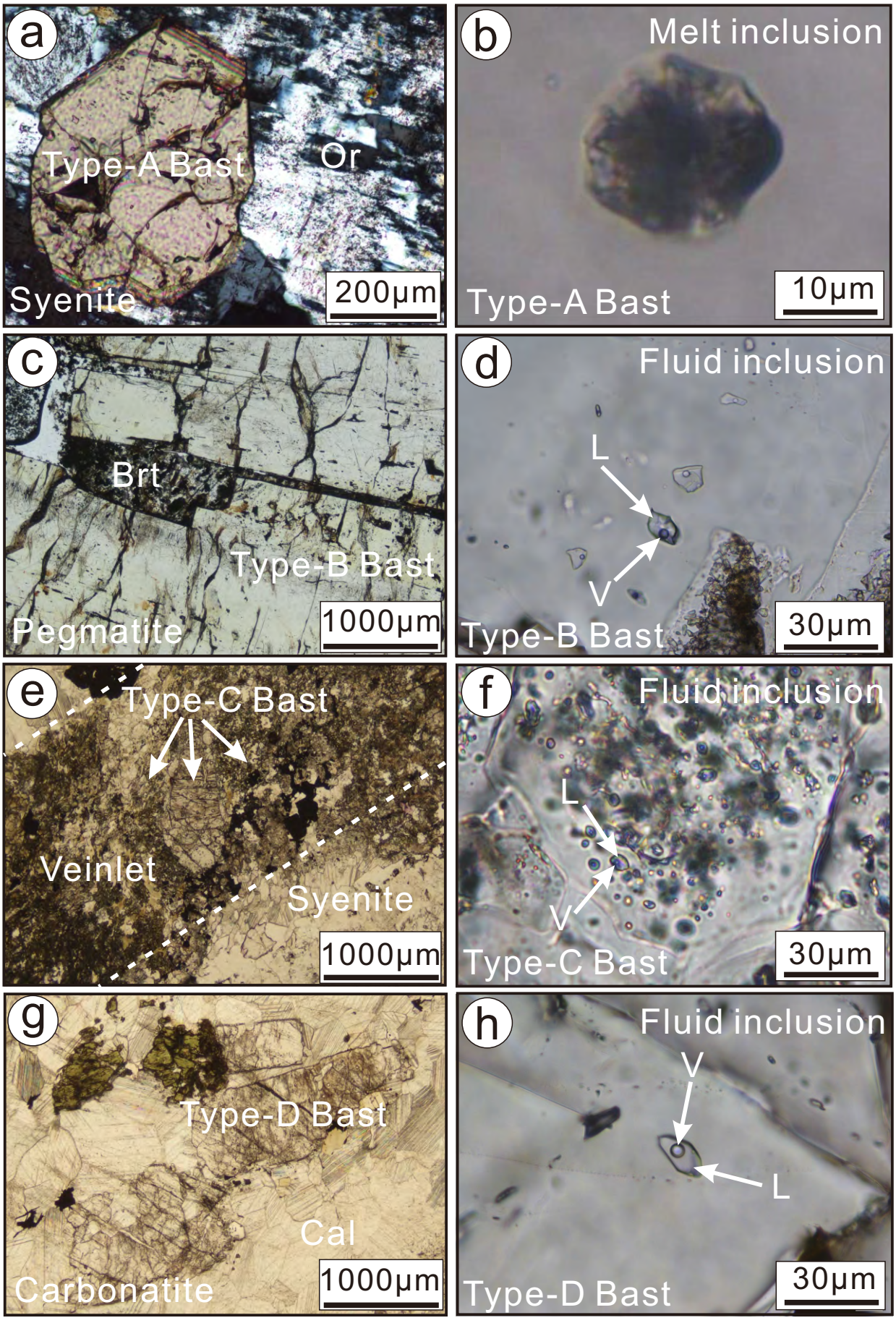

Figure 4

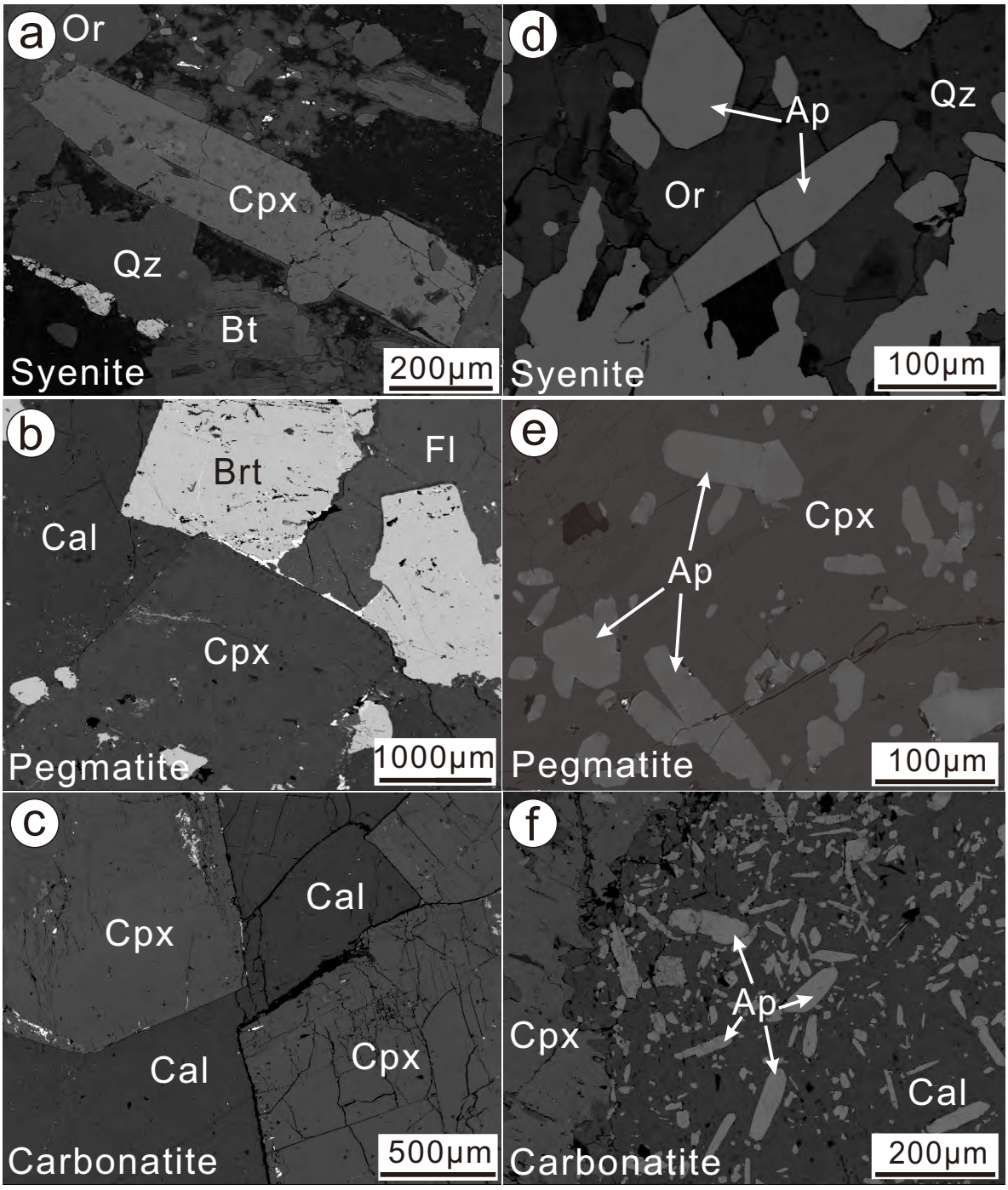

Figure 5

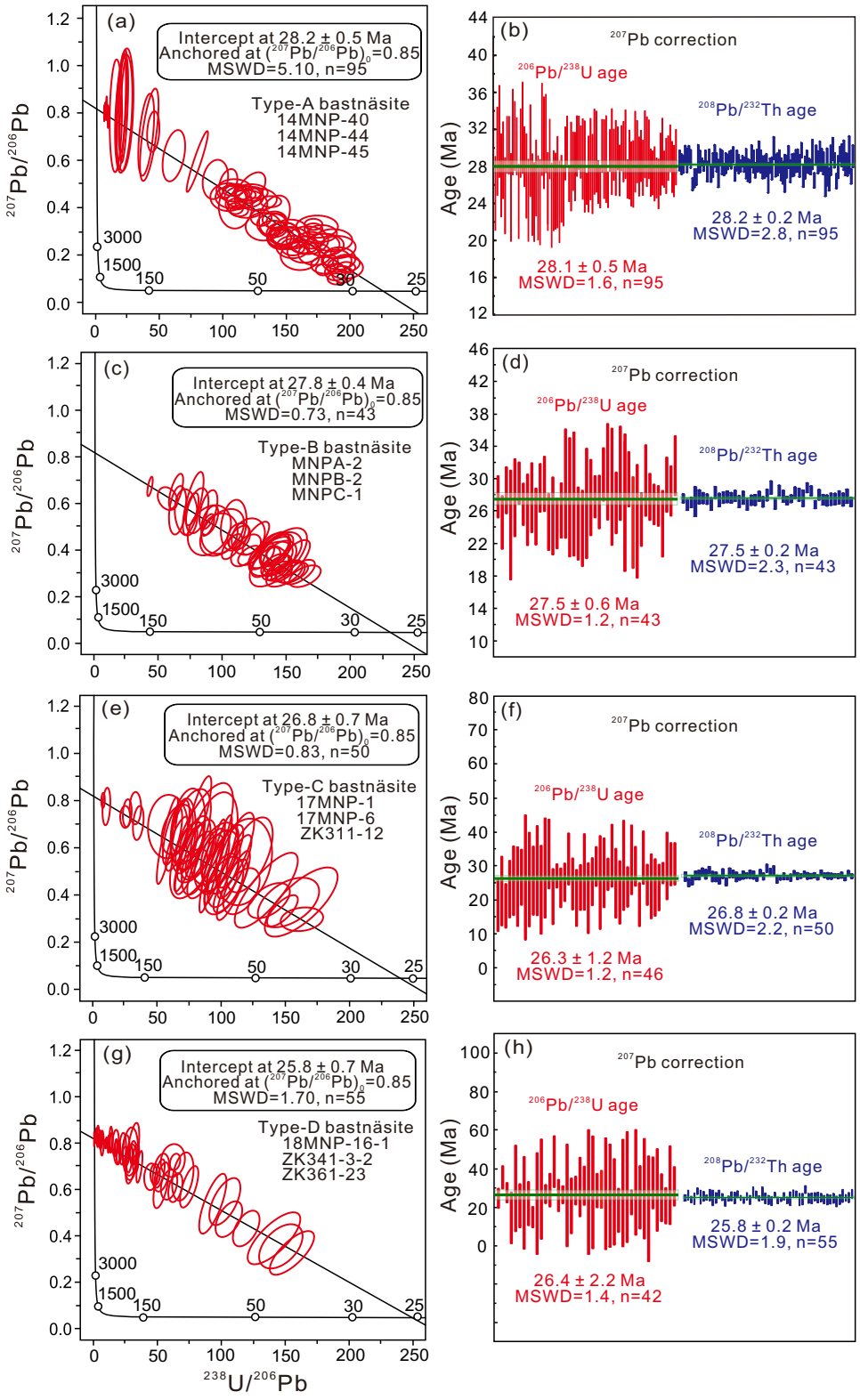

This is the peer-reviewed, final accepted version for American Mineralogist, published by the Mineralogical Society of America.
The published version is subject to change. Cite as Authors (Year) Title. American Mineralogist, in press.
DOI: https://doi.org/10.2138/am-2021-7778. http://www.minsocam.org/

Figure 6

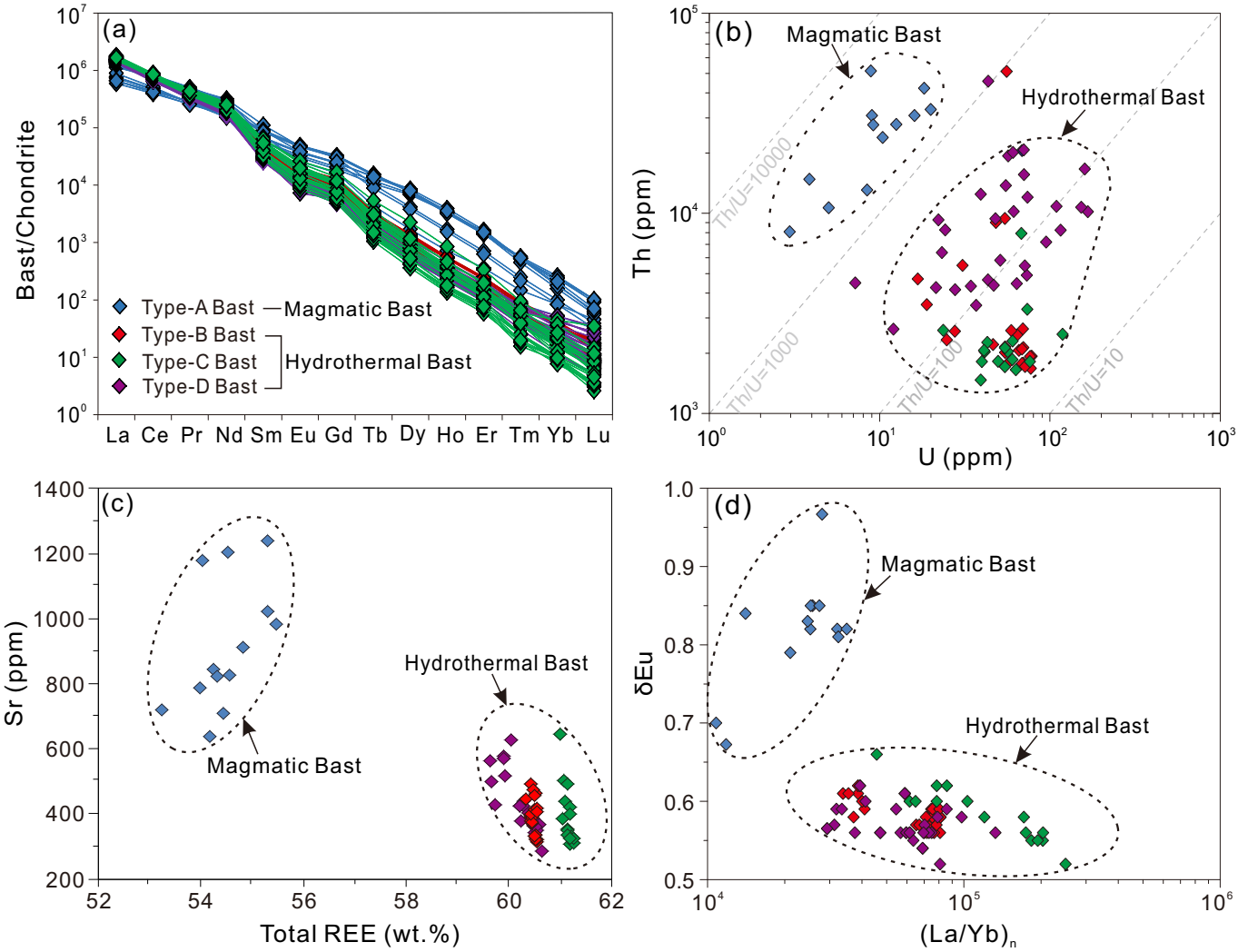

Figure 7

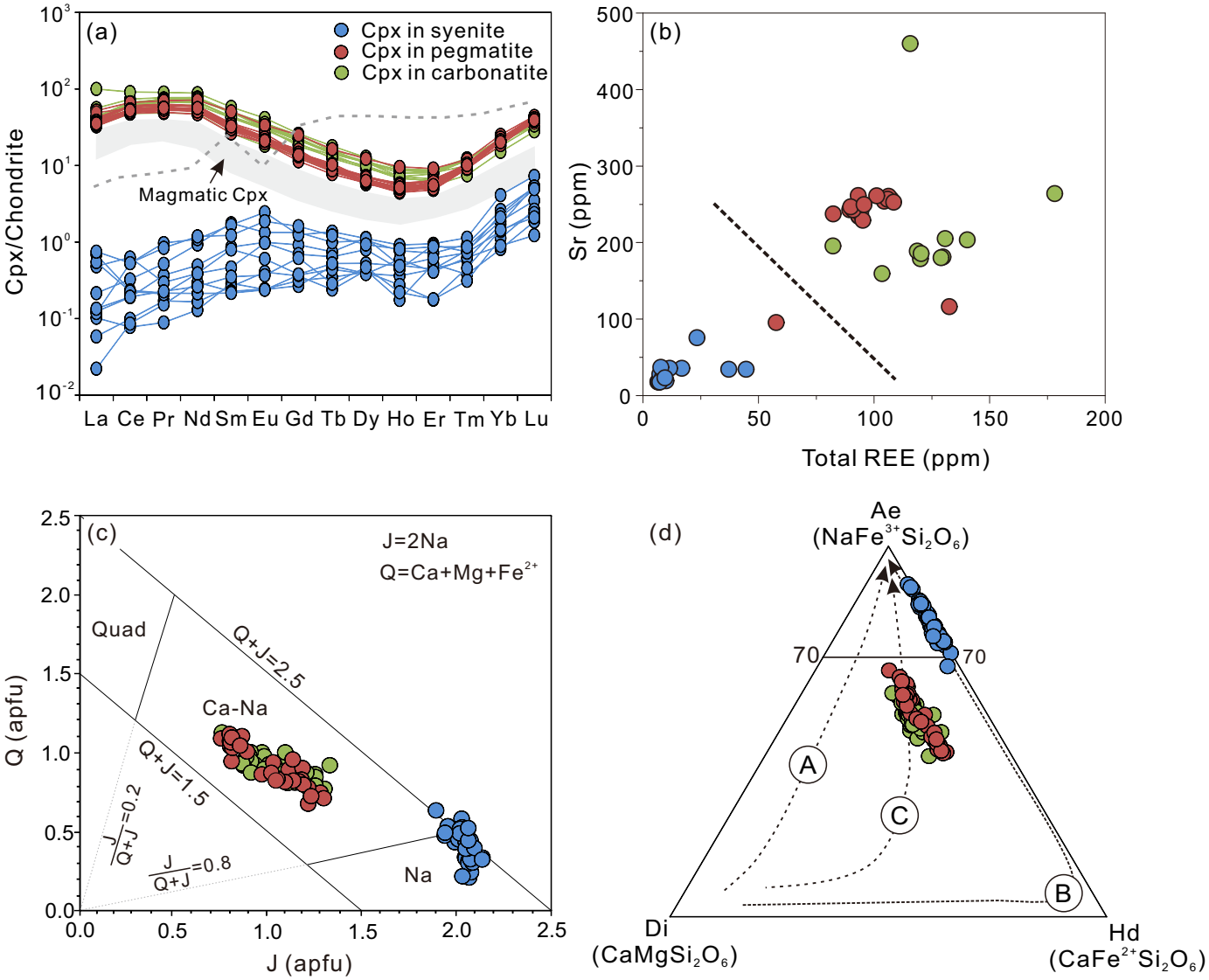

This is the peer-reviewed, final accepted version for American Mineralogist, published by the Mineralogical Society of America.
The published version is subject to change. Cite as Authors (Year) Title. American Mineralogist, in press.
DOI: https://doi.org/10.2138/am-2021-7778. http://www.minsocam.org/

Figure 8

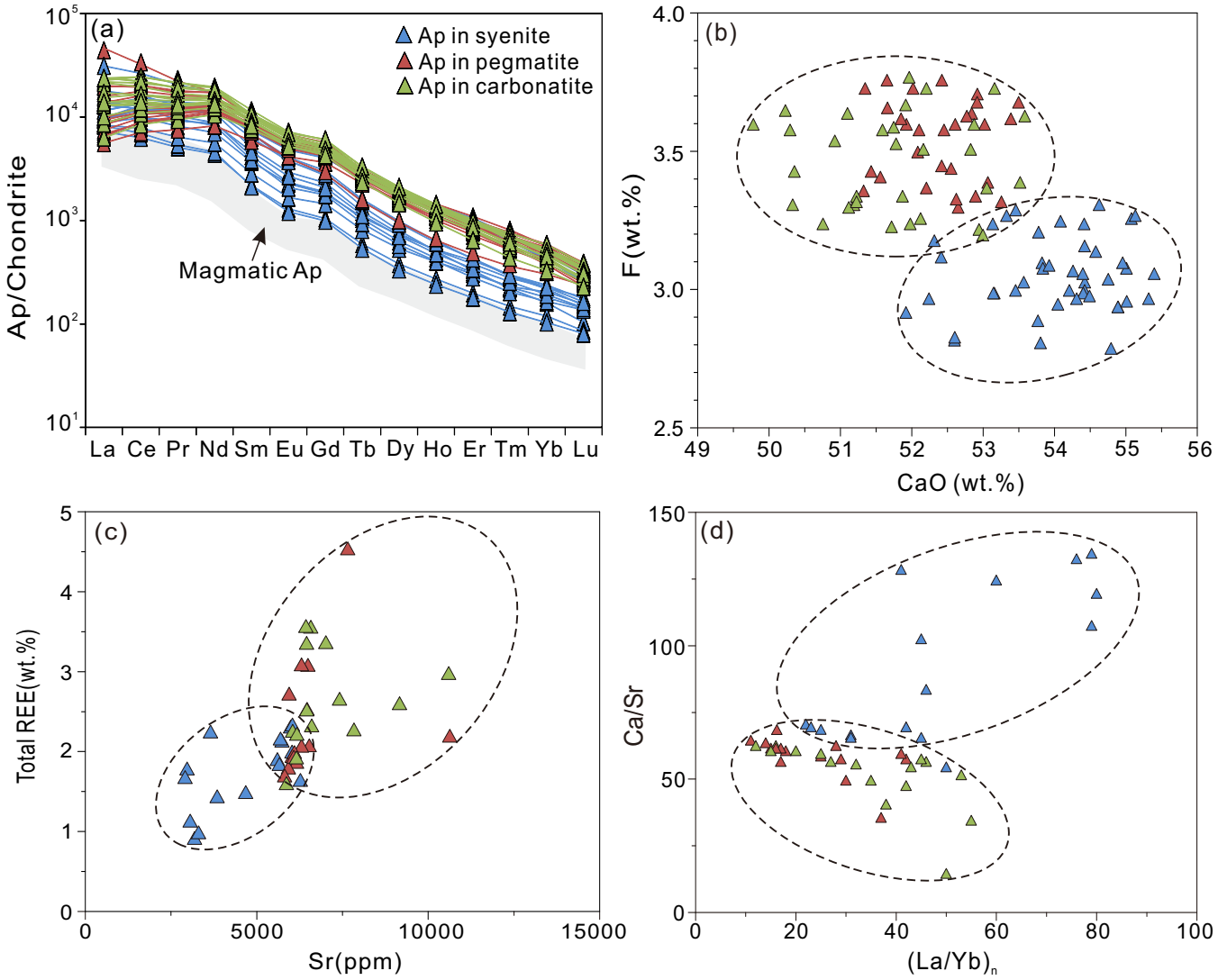

Figure 9